THE UNIVERSITY OF
WARWICK

warwickpublicationswrap

highlight your research

http://wrap.warwick.ac.uk/

ARTICLE TYPE

High Resolution Mapping of Oxygen Reduction Reaction Kinetics at Polycrystalline Platinum Electrodes

Chang-Hui Chen,[a] Katherine E. Meadows,[a] Anatolii Cuharuc,[a] Stanley C. S. Lai,[a,b] and Patrick R. Unwin[a,*]

The scanning droplet-based technique, scanning electrochemical cell microscopy (SECCM), combined with electron backscatter diffraction (EBSD), is demonstrated as a powerful approach for visualizing surface structure effects on the rate of the oxygen reduction reaction (ORR) at polycrystalline platinum
10 electrodes. Elucidating the effect of electrode structure on the ORR is of major interest in connection to electrocatalysis for energy-related applications. The attributes of the approach herein stem from: (i) the ease with which the polycrystalline substrate electrode can be prepared; (ii) the wide range of surface character open to study; (iii) the possibility of mapping reactivity within a particular facet (or grain), in a *pseudo-single crystal* approach, and acquiring a high volume of data as a consequence; (iv) the ready
15 ability to measure the activity at grain boundaries; and (v) an experimental arrangement (SECCM) that mimics the three-phase boundary in low temperature fuel cells. The kinetics of the ORR was analyzed and a finite element model was developed to explore the effect of the three-phase boundary, in particular to examine pH variations in the droplet and the differential transport rates of the reactants and products. We have found a significant variation of activity across the platinum substrate, inherently linked to the
20 crystallographic orientation, but do not detect any enhanced activity at grain boundaries. Grains with (111) and (100) contributions exhibit considerably higher activity than those with (110) and (100) contributions. These results, which can be explained by reference to previous single crystal measurements, enhance our understanding of ORR structure-activity relationships on complex high-index platinum surfaces, and further demonstrate the power of high resolution flux imaging techniques to
25 visualize and understand complex electrocatalyst materials.

Introduction

30 The oxygen reduction reaction (ORR) is a key reaction in low temperature fuel cells[1-3] and lithium-air batteries,[4, 5] and is arguably a major limiting factor, at least from a scientific point of view, to the widespread adoption of these technologies. However, even on the best catalysts (Pt and Pt-based materials), the ORR
35 suffers from sluggish kinetics and requires a high overpotential. The mechanism and kinetics of the ORR on Pt have been studied[6-8] to understand the cause of the sub-optimal performance and to identify strategies to optimize the catalytic properties of Pt surfaces.[9-11] A common strategy is to identify the most efficient
40 surface structure for the ORR and then try to expose these micro- or nano-structures in the catalysts.[10] To do this, knowledge of the structure-dependence of the ORR activity is required. Previous research on a variety of Pt-based materials, spanning bulk polycrystalline electrodes,[12, 13] single-crystal electrodes[14, 15] and

45 nanoparticles,[2, 16] has shown that the ORR kinetics and mechanism are strongly affected by the nature and the structure of electrodes. Importantly, research on atomically well-defined single-crystal electrodes has revealed a strong crystallographic orientation dependence of the ORR activity.[9, 14, 17, 18]

50 The catalytic activity of the ORR on the three basal planes of Pt has been investigated widely in different electrolytes.[19-23] In sulfuric acid, the reactivity of the Pt basal planes decreases in the order $(110) > (100) > (111)$,[20] following the relative adsorption strength of the sulfate anion. These studies have been augmented
55 by research on stepped Pt surfaces in the $[01\bar{1}]$ and $[1\bar{1}0]$ zones, showing that these have higher activity than the basal planes. Recently, this has been rationalized by using the OH binding energy as a descriptor for activity, yielding a volcano-relationship.[24] Similar relative reactivity patterns have been found
60 in non-specific adsorbing perchlorate electrolyte, although the variation in activities is much smaller.[17, 18]

While single-crystal electrodes provide valuable information on systematic trends, the availability of surfaces can be limited, with high-index surfaces particularly challenging to prepare and maintain. Furthermore, the activity of grain boundaries, which are present in real catalysts and on polycrystalline electrodes, cannot be studied on single-crystal surfaces, even though these features have been suggested to play a large role in real catalysts.[25, 26] For example, we have shown recently that the $Fe^{2+/3+}$ redox process on polycrystalline platinum electrodes in sulfuric acid is dominated by grain boundaries.[27] To evaluate whether similar effects operate for the ORR, localized electrochemical measurements are needed, as reported herein.

In contrast to the extensive studies on Pt basal surfaces, and, to some extent, stepped surfaces, less is known about the ORR on high-index surfaces. However, real surfaces, as presented in bulk electrodes and nanoparticles, are usually heterogeneous in the crystallographic structure and combine different facets and surface features, such as atomic steps and kinks.[28] Moreover, some high-index surfaces, which have high densities of steps and kinks,[28] are reported to exhibit higher electrocatalytic activity than basal planes.[29, 30] Therefore, more research on high-index Pt surfaces is essential to gain a better understanding of the structure sensitivity of ORR.

The studies in this paper draw on our recently reported *pseudo-single-crystal* approach, in which scanning electrochemical cell microscopy (SECCM)[27, 31-38] is used to probe local electrochemical activity that is correlated with the local surface structure provided by electron backscatter diffraction (EBSD).[39] This approach has several key attributes. First, minimal sample preparation is required. Second, grains of high-index orientation, which are not easily prepared as single-crystal electrodes, can be studied, and activity can be mapped within a grain, in a *pseudo-single crystal* approach. Third, enhanced activity at grain boundaries can be detected directly based on the scanning mode of SECCM.[27] Finally, for the ORR, SECCM provides a relevant configuration with a three-phase boundary between the solid electrode, liquid electrolyte and gaseous oxygen (air), which mimics the geometry present at the cathode of low temperature fuel cells. This configuration leads to greatly enhanced mass transport of oxygen to the electrode surface, as oxygen is not only provided through the electrolyte solution but also across the liquid-air interface to the electrode surface, while (solution-phase) reaction products can only be transported away from the electrode surface through the electrolyte solution at a slower rate. The impact of this differential mass transport between reactants and products on the ORR kinetics has only rarely been investigated,[40] but is open to study with the approach herein.

Materials and Methods

Chemicals and Materials. H_2SO_4 (99.999 % purity, Sigma-Aldrich) and KCl (Sigma-Aldrich) solutions were prepared by using high purity water (Milli-Q, Millipore, 18.2 MΩ cm resistivity at 25 °C). A piece of polycrystalline Pt foil (> 99.95 %, 0.0125 mm thickness; Advent Research Materials) was used as the substrate. Palladium wires (> 99.95 %, MaTeck) were used to prepare the quasi-reference counter electrodes (QRCEs) for the SECCM setup.

Preparation of QRCEs. The palladium-hydrogen (Pd-H_2, $E^0 =$ +50 mV vs. reversible hydrogen electrode (RHE))[41] QRCEs were prepared by applying a -3.0 V bias between the palladium electrode and a Pt wire counter electrode in a two electrode setup in 0.05 M sulfuric acid, driving the hydrogen evolution reaction on the palladium electrode. The bias was held until a stable current was attained and bubbles were visible on the palladium wire, indicating that the palladium wire was saturated with H_2.

Preparation of the Pt substrate electrode. Before performing SECCM experiments, the Pt foil was cleaned by flame annealing, followed by repeated voltammetric cycling in 0.05 M H_2SO_4 solution (between 0.0 V and 1.5 V vs. RHE, finishing at 0.0 V with a scan rate of 100 mV s^{-1}) to ensure a clean surface, as witnessed by a stable voltammogram with well-defined hydrogen underpotential deposition (H_{UPD}) features.[42] The Pt foil was then immediately transferred to the SECCM instrument and covered by a droplet of dilute sulfuric acid (ca. 25 μL on a 0.4 cm × 0.5 cm platinum foil) to minimize surface contamination. The droplet was removed just before performing SECCM measurements.

Pipette fabrication and meniscus size measurement. SECCM pipettes were pulled from borosilicate theta capillaries (TG 150-10, Harvard Part No. 30-0114) using a Sutter P-2000 laser puller (Sutter Instruments, USA). The outer walls of the pipettes were silanized with dichlorodimethylsilane (99+ % purity, Acros) to increase the hydrophobicity. The size and geometry of the pipettes at the end was measured on a Zeiss SUPRA 55 variable-pressure field emission-scanning electron microscope (FE-SEM). The taper angles of the pipettes were measured by FE-SEM, and ranged from 6.5 ° ~ 8.5 °.[34]

The contact area of the meniscus was determined by filling a pipette, of the same size as used for imaging, with 50 mM KCl solution and bringing it into contact with the platinum surface. The pipette was allowed to stay there for several minutes and then retracted, leaving a droplet of solution that upon drying produced a residue of KCl crystals. The meniscus footprint was then measured by FE-SEM.

SECCM setup. The SECCM setup has been reported in detail in our recent papers.[27, 31-36] A schematic of the SECCM setup is shown in Figure 1A. In short, the electrolyte meniscus at the end of a tapered dual-barrel pipette was used as a mobile electrochemical cell. After filling with electrolyte solution (0.05 M H_2SO_4), Pd-H_2 QRCEs were inserted into each channel of the theta pipette. A potential bias (V_2) was applied between the two QCREs to induce an ion conductance current (i_{dc}) across the meniscus, which aided tip positioning and imaging. The pipette was mounted on a *z*-piezoelectric positioner to which a periodic oscillation (normal to the substrate) was applied (60 nm peak amplitude at 233 Hz). This oscillation produced an alternating current component (i_{ac}) in the conductance current through the meniscus, when the meniscus was in contact with the substrate, providing a highly sensitive feedback signal that was used to maintain a stable contact between the droplet and the substrate.[31, 34] The magnitude of the i_{ac} set point for the studies in this paper was in the range of 1.6 % ~2.0 % of the i_{dc} value.

A piece of polycrystalline Pt foil, containing a variety of grains, was mounted on an *x-y* positioner and used as the substrate. The Pt foil was connected to a high sensitivity current
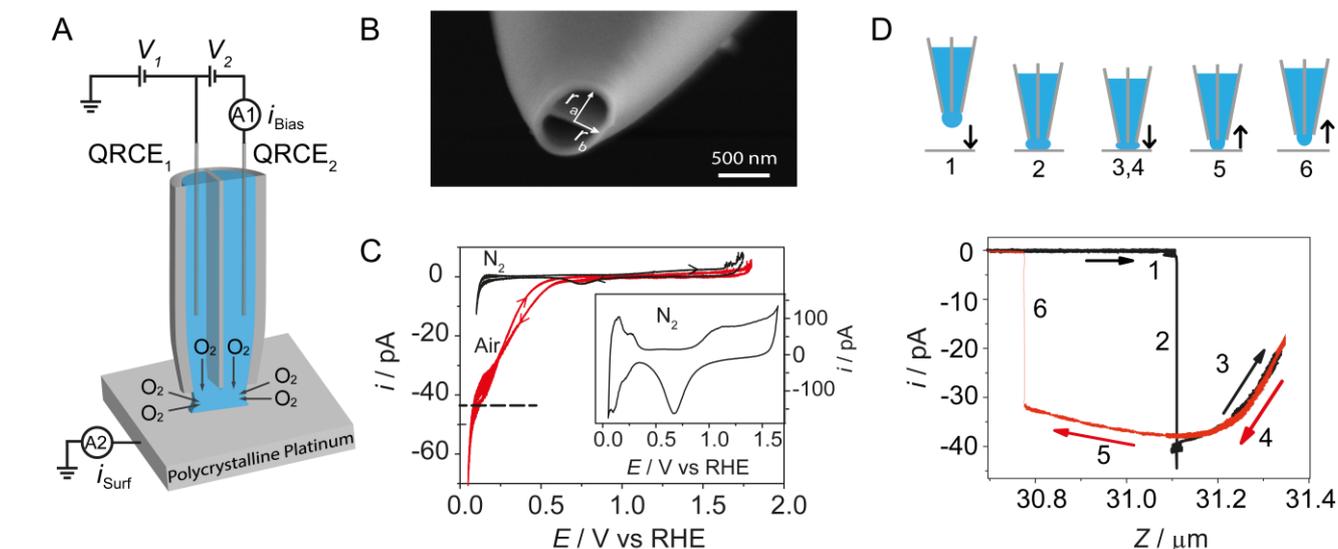
ARTICLE TYPE

Figure 1. (A) Schematic of the SECCM setup. A Pd-H$_2$ quasi-reference counter electrode (QRCE) was inserted into each channel of the pipette, filled with 0.05 M H$_2$SO$_4$. A bias potential, V_2, was applied between the two QRCEs and the resulting ion conductance current (i_{Bias}) between the two channels was measured. A potential, V_1, relative to ground, was applied to QRCE$_1$; and the effective working electrode potential (at ground) was - ($V_1 + V_2 / 2$) vs.
5 Pd-H$_2$, against which the working electrode current, i_{Surf}, was measured. (B) FE-SEM image of a pipette used for SECCM imaging. r_a and r_b are the major and minor inner radius of the pipette opening. (C) SECCM cyclic voltammograms (CVs) of a polycrystalline Pt electrode in a deaerated (nitrogen-purged) solution (black line) and in air for the ORR (red line) at a scan speed of 50 mV s^{-1}. The diffusion-limited current is indicated by the horizontal black dashed line for ease of reference. The inset (current values shown in the right axis) is a blank CV recorded in a deaerated solution at a scan speed of 5 V s^{-1}.
^{1}. (D) Typical surface electrochemical current response for the ORR on a polycrystalline Pt electrode in 0.05 M H$_2$SO$_4$ at 0.20 V relative to RHE (close to
10 the diffusion-limit for the ORR) as: 1, the pipette approached the surface; 2, the meniscus contacted the surface; 3, the meniscus was squeezed; 4 and 5, pipette retracted from the surface; 6, the meniscus detached. The cartoon illustrates the pipette and droplet position at these different stages.

amplifier. By moving the meniscus across the substrate, electrochemical activity images for the substrate at different
15 applied potentials (adjustment of V_1) can be obtained. To a good approximation the substrate potential is - ($V_1 + V_2 / 2$).[31, 34] All potentials herein are reported for the substrate electrode relative to the reversible hydrogen electrode (RHE).

The entire setup was placed in a Faraday cage to minimize
20 electronic noise. To perform the measurement without oxygen present, the substrate and pipette were placed in an environmental chamber where nitrogen gas (passed through a glass vessel containing water) was flowed through continuously to remove the dissolved oxygen in the meniscus, as reported before.[43]
25 The meniscus height during SECCM imaging can be estimated by combining the i_{dc} and i_{ac} value and using Finite Element Method (FEM) modelling.[36, 38] For the pipettes used herein for SECCM scanning, the estimated meniscus height was 150 nm.

EBSD experiments. EBSD images of Pt substrates were
30 recorded on a Zeiss SUPRA 55 variable-pressure FE-SEM equipped with an EDAX TSL EBSD system. The measurements were carried out at 20 kV on a sample tilted at 70 °. Data were acquired every 1.5 μm across the substrate and analyzed with commercial orientation imaging microscopy (OIM) software. The
35 data were represented with color coded orientation maps.

Results and Discussion

Figure 1A shows a schematic of the setup for SECCM, illustrating the meniscus at the end of the pipette which results in a three phase boundary configuration, so that there is diffusion of
40 oxygen down the two barrels of the pipette as well as from the edge of the droplet across the air-aqueous interface. Figure 1B shows a representative FE-SEM image of the pipette used in SECCM measurement. All the pipettes used herein were pulled from double-barrelled (theta) capillaries, creating openings at the
45 end of the pipettes that were about 700-800 nm diameter.

Typical cyclic voltammograms (CVs) recorded in the SECCM setup using a pipette filled with 0.05 M H$_2$SO$_4$ at a polycrystalline platinum foil electrode are shown in Figure 1C. In the main figure, the black line is an SECCM CV recorded under nitrogen
50 flow in an environmental chamber between 0.05 V (starting and end potential) and 1.75 V (reverse potential) at a scan speed of 50 mV s^{-1}. The red line refers to the ORR CV recorded at the same starting potential but slightly higher reverse potential (1.8 V) at the same scan speed in air. In the ORR CV, there is a small
55 hysteresis between the forward and reverse waves because the forward wave starts at a cathodic potential (0.05 V) where the surface is covered in adsorbed hydrogen (and is evolving
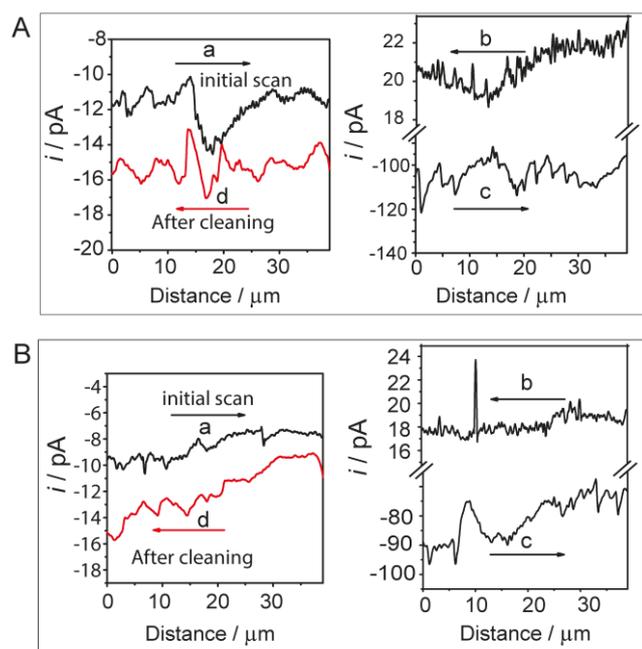
Figure 2. Experimental data of two separate series of line scans in 0.05 M H₂SO₄ (shown in Figure 2A and Figure 2B respectively). Each line was scanned four times at different potentials relative to the reversible hydrogen electrode (RHE) : a, 0.45 V; b, 1.25 V; c, 0.05 V; and d, 0.45 V. Numbers in the figures and the arrows represent the sequence and direction of scanning.

hydrogen) whereas for the reverse wave, the surface is oxide covered before the ORR commences. Comparing the two CVs, it is clear that significant currents due to the ORR are observed at potentials below ca. 0.7 V, a potential region at which oxide reduction processes typically occur. The inset in the figure shows another SECCM CV recorded under nitrogen flow at a higher scan speed of 5 V s⁻¹. The characteristic platinum features can been seen,[42] similar to CVs obtained under conventional conditions (see ESI, section 1), validating the SECCM experimental setup and highlights that the as-prepared substrate remain clean.

Notably, the ORR CV is recorded under high mass transport conditions (k_t ~ 0.1 cm s⁻¹), which is about an order of magnitude higher than conventional electrochemical measurement, e.g. using a rotating disk electrode. The high mass transport of SECCM serves to push the ORR diffusion-limited current to more cathodic potentials. Recently, Kucernak and co-workers have reported similar cathodic shifts for the ORR measurement on Pt nanoparticles under high mass transport conditions.[44, 45]

For the ORR, the flux of oxygen is provided by diffusion down the barrels of the pipette into the electrolyte meniscus as well as across the air-water interface of the meniscus (Figure 1A), which is a rapid process.[46] Consequently, the diffusion-limited current (approximately 40 - 45 pA as marked by dashed line in Figure 1C) is much higher than would be expected if diffusion was only due to O₂ initially in solution (ca. 27 pA based on meniscus height of 150 nm, see ESI, section 2). This is an interesting feature of SECCM, opening up studies of ORR in the presence of a three-phase boundary, and with the possibility of controlling mass transport rates by changing the meniscus height, as we discuss herein.
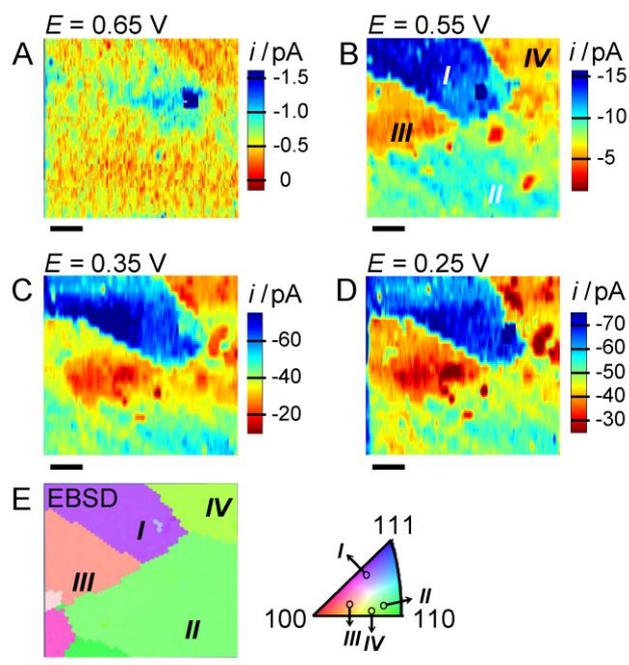

Figure 3. SECCM surface current images (A-D) and the corresponding EBSD image (E) of one area of a Pt electrode. Electrochemical current images at 0.65 V (A), 0.55 V (B), 0.35 V (C) and 0.25 V (D) relative to RHE in 0.05 M H₂SO₄. Labels "*I*", "*II*", "*III*" and "*IV*" (in (B) and (E)) highlight four characteristic grains. The scale bar is 10 µm.

The impact of the meniscus geometry on the ORR current was investigated through experiments in which the meniscus height was varied while measuring the diffusion-limited oxygen current, as illustrated in Figure 1D. Initially, the droplet at the end of the pipette was brought into contact with the surface held at 0.2 V (close to the mass transport-limited potential) at a speed of 1.5 µm s⁻¹ (label 1 in Figure 1D). Once surface meniscus contact was established (label 2), as a jump to contact, there was rapid establishment of the ORR diffusion-limited current. Once this was sensed, the tip translation speed towards the substrate changed automatically to a much slower value as the tip was further lowered (20 nm s⁻¹, label 3), decreasing the tip-to-substrate separation, or similarly, squeezing the meniscus height, for a total distance of 250 nm. Clearly, squeezing the meniscus decreases the area of the air/water interface and consequently diminishes the flux of O₂ to the Pt surface as evident in the gradual decrease of the mass transport-limited current. Before the pipette made physical contact with the surface, the motion was reversed, increasing the tip-to-substrate separation (meniscus height) It can be seen that the ORR current during the retraction of the pipette initially closely follows that during squeezing with little hysteresis (label 4). However, detachment (label 6) does not occur at the same *z* position as attachment (label 2). Rather, the pipette has to be pulled back an additional 300 nm (label 5) before liquid meniscus detachment from the surface. This is reminiscent of AFM force curves in air where there is a strong attractive interaction between the tip and the substrate due to capillary forces.[47, 48] During this pull-off period, there was a small decrease in the limiting current, which might be a consequence of a small decrease in the contact area of the meniscus with the surface.
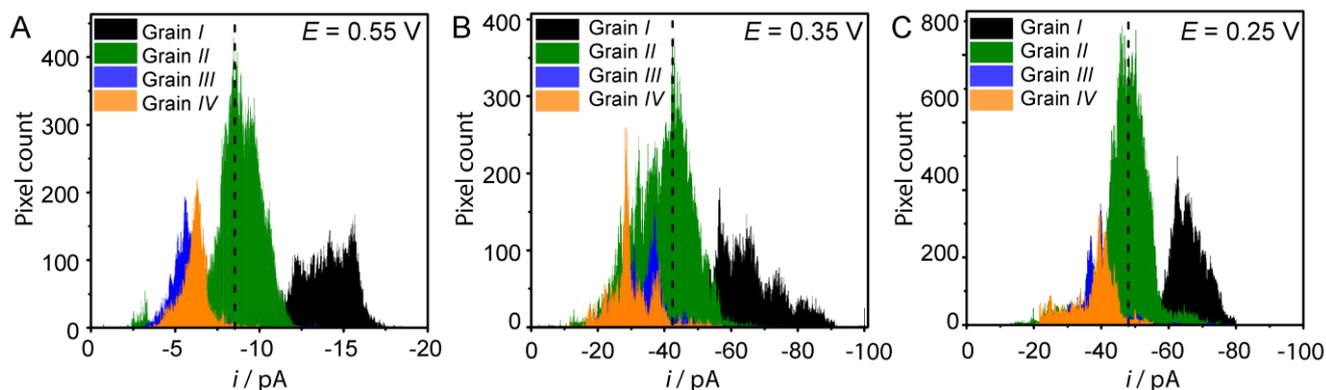
ARTICLE TYPE

Figure 4. Histograms of electrochemical current distribution for ORR on the four labeled grains in Figure 3 at a Pt electrode potential of 0.55 V (A), 0.35 V (B), and 0.25 V (C) relative to RHE in 0.05 M H_2SO_4. The dashed line in each figure indicates the average current at that potential. These histograms were obtained by analyzing the data at individual pixels from regions where grains were identified on the SECCM images.

For the present studies, up to about one hour could elapse between preparing the sample (albeit with protection from the electrolyte for part of the time) and finally landing the meniscus for SECCM imaging. Since the ORR could be susceptible to contamination, additional checks were performed that there was no significant change in the surface quality from atmospheric contamination.   To do this, we performed SECCM line scan experiments on different areas of the Pt foil, in which each line was scanned four times with the meniscus at different potentials. Typical sets of current profiles on two different areas are shown in Figures 2A and 2B. After the electrolyte meniscus was brought into contact with the as-prepared surface as usual, a meniscus linescan across 40 μm at a speed of 0.5 μm s^{-1} was carried out four times over the same area of the surface. For the first (label a) and last pass (label d), the potential was held at the value of interest (0.45 V, well removed from the diffusion-limited potential to ensure that any impact of changes in the surface kinetics would be seen). In the second pass (label b), a potential of 1.25 V was applied which would readily oxidize any surface contaminants. On the third pass (label c), the potential was held at 0.05 V to reduce the surface oxides formed on the second pass. By comparing the ORR current for the first pass (sample as prepared) and the fourth pass (sample as prepared plus *in situ* electrochemical cleaning), the effect of the two areas at 0.45 V was found to be about 20-30 %, which is small compared to the several-fold change in activity that we observe between grains (*vide infra*). It was found that similar current features were observed without and with additional cleaning. This indicates that the method of surface preparation and SECCM analysis yields a relatively clean surface with minimal impact of surface contamination on electrochemical activity over the duration of the imaging measurements. Importantly, this aspect was further evident from the images reported herein in which there was no obvious deterioration in surface electrochemical current during the course of a scan (*vide infra*).

To investigate the influence of structure on ORR activity, SECCM imaging experiments were performed. For this experiment, the dimensions of the pipette and the footprint of the droplet were measured precisely by FE-SEM. The SEM measurement (Figure 1B) showed that the pipette used for SECCM imaging had an elliptical end opening, with a major inner radius r_a = 370 nm and minor inner radius r_b = 260 nm. The footprint measurement showed a droplet contact with major and minor semiaxes, r_{ma} and r_{mb}, of 650 nm and 520 nm, respectively, resulting in a contact area of 1.06×10^{-8} cm^2. This is typical for SECCM.[31, 34] SECCM activity images on a typical area of Pt held at four different substrate potentials, 0.65 V, 0.55 V, 0.35 V and 0.25 V in 0.05 M H_2SO_4 are shown in Figures 3A, B, C and D, respectively. Note that the data were acquired in a random order (in the sequence of 0.55 V, 0.25 V, 0.65 V and 0.45 V) to avoid any systematic error. For this area, data were acquired every 6.5 nm along a particular line with a spacing of 2.5 μm between lines. The crystallographic orientation of the same area was obtained by EBSD and is shown as an inverse pole plot in Figure 3E. In the colour legend, the three corners of the triangle represent the three basal planes of Pt. The facets which are located on the side-lines are vicinal (or stepped) planes, while the inside of the triangle represents high-index (or kinked) planes. The EBSD image indicates that all of the grains in the scanned area are high-index orientations of distinctly different structure. Comparing the SECCM images with the EBSD results, four main grains can be identified, labelled as grain *I*, *II*, *III* and *IV*. The correlation between the electrochemistry and surface structure is discussed below.

The large amount of data obtained from SECCM allows further quantitative analysis of the images. Histograms of the electrochemical current for the grains in Figure 3 at 0.55 V, 0.35 V and 0.25 V are shown in Figures 4A, B and C, respectively. At each potential, the electrochemical current distribution was plotted by extracting data from the individual grains in the SECCM images. The black vertical dashed line in each histogram indicates the average current over the entire scanned area at that potential. The relative activity for the four main grains is always in the order *I* > *II* > *III* ≈ *IV*. Moreover, the current distribution

for each grain is rather broad, which can be attributed to the complex structure of the grains, which have contributions from all three basal planes in different proportions, rather than being perfect single crystal surfaces. It is important to point out that variations in activity due to the variations in wetting can be ruled out, as the complementary ion conductance direct and alternating current images (see ESI, section 3) show that all the grains wet to the same level. In addition, the activity features observed are not due to variations in the roughness of the platinum foil, which is negligible, as discussed in our previous work.[27]
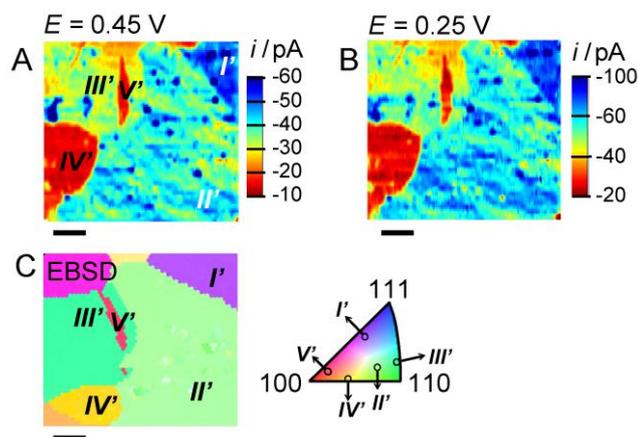

Figure 5. Electrochemical current images at 0.45 V (A) and 0.25 V (B) relative to RHE in 0.05 M H₂SO₄ and the corresponding EBSD image (C) for an area of a Pt electrode. The orientations of the five labeled grains are also marked on the color coded orientation map to guide the reader. The scale bar is 10 μm.

To support the data above, and obtain more detail, higher resolution images were acquired, again with a resolution of 6.5 nm for each pixel in the line, but with a spacing of 1 μm between each line. Images of the electrochemical activity at 0.45 V and 0.25 V are presented in Figures 5A and 5B, while the crystallographic orientations of the grains in this area are shown in Figure 5C. In this case, SECCM images combined with EBSD maps allowed us to identify five regions with different activities and assign these to individual grains (*I'*, *II'*, *III'*, *IV'* and *V'*). Here the experiment employed a thicker meniscus, as evidenced by the higher ion conductance current (~ 27.5 nA), which means more influence of oxygen transport through the water/air interface (following from Figure 1D), and so higher electrochemical substrate currents, especially in the limiting current region.

In Figure 3 and Figure 5, comparison of SECCM images and EBSD maps shows a strong correlation between variations in electrochemical activity and the grain structure. Specifically, grain *I* (Figure 3) and grain *I'* (Figure 5), which have (100) and (111) characteristics, exhibit the highest activity among all the grains. In the map recorded at a low driving potential, 0.65 V (Figure 3A), grain *I* can still clearly be distinguished, even when the currents from the other grains are negligible. In general, among the other grains, which are located close to (but not on) the bottom side of the colour legend triangle there are two categories: those close to the (110) basal plane exhibit higher activities than those close to the (100) plane. Thus, in Figure 3, grain *II* is more active than grain *III* and grain *IV*, while in Figure

5, grain *II'* and grain *III'* exhibit higher activity than grain *IV'* and grain *V'*. Finally, grains close to the (100) orientation exhibit the lowest activity among all the investigated grains and the difference among them is much smaller.
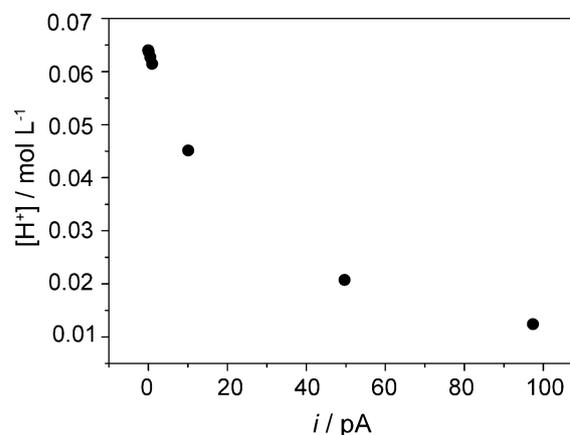

Figure 6. Proton concentration near the electrode surface vs. surface electrochemical current for the ORR from FEM simulations.

In summary, SECCM images combined with EBSD data demonstrate that ORR activity varies strongly with the crystallographic orientations of high-index Pt grains. The relative activity trend holds throughout the entire (wide) potential range investigated. Notably, the current value varies by several-fold for different grains across a small area of the surface (60 μm × 60 μm). Based on research on single-crystal basal planes, the adsorption of (bi)sulfate on (111) long range terraces strongly hinders the ORR, while the introduction of mono-atomic steps on the surface, enhances the activity by breaking the long range order and thereby the anion adsorption strength.[10, 49] Our results are consistent with this analysis, showing that facets close to (111) orientation with (100) contributions are the most active.

Although a possible role of grain boundaries for the ORR has been discussed in a few papers on nanocrystalline particles,[26, 50] we do not see any obvious enhanced activities at grain boundaries. SECCM is capable of visualizing such enhancements in activity[27] although the grain boundary activity needs to be much higher than that of the grain in order for it to be detected.

To further assess the SECCM data and validate the approach in comparison to other techniques, a simple kinetic analysis was performed at 0.55 V, where the current is mostly under kinetic control and where perturbations of the solution composition in the meniscus are also less severe than at more driving potentials.

Although the ORR current is essentially under kinetic control, we corrected for minor mass transport effects. The relationship between the observed current density (j), the kinetic current density (j_k), and the mass transport-limited current density (j_d) is reasonably given by:

$$\frac{1}{j} = \frac{1}{j_k} + \frac{1}{j_d} \tag{1}$$

which yields the following for j_k,

$$j_k = \frac{jj_d}{j_d - j} \qquad (2)$$

Current densities were obtained by dividing measured currents by the contact area of the electrolyte meniscus (*vide supra*). We take j_d to be 6.2 mA cm^{-2}, based on the average current in the major active grain *I* in Figure 3 (65.4 pA) at a potential of 0.25 V which corresponds to the mass transport-limited potential. At 0.55 V, the average *j* is 810 µA cm^{-2} (based on the average current, *i* = 8.6 pA, across the entire scanned area). By solving equation 2, an average j_k of 932 µA cm^{-2} was obtained. Evidently, the current values depicted in Figures 3B and 4A, approximate well to kinetic values, with minimal mass transport contribution.

The current densities we measure are broadly in line with, although a little lower than, previous studies.[44] In large part, this can be attributed to our three-phase system that results in differential mass transport of the reactant O$_2$ (which is provided down the barrels of the pipette and across the electrolyte-air interface) versus the flux of solution-phase products (such as H$^+$ and H$_2$O$_2$, which can only diffuse to and from the electrode in barrels of the pipette). To gain some insights into the impact of the three-phase system on mass transport, a finite element method model was developed (see ESI, section 2). With this model, we were able to predict the electrochemical currents (with specific electrode kinetics), and the resulting average proton concentration in the solution near the electrode surface. Notably, Figure 6 shows that the proton concentration near the electrode decreases sharply with increasing electrochemical current (kinetics). The depleted proton concentration decreases the effective applied overpotential at the electrode-electrolyte interface (through a shift in the equilibrium potential), thereby reducing the driving force and the observed current. This mismatch between oxygen and proton transport pathways, resulting in proton depletion at the three-phase boundary can also be a major issue in fuel cells, particularly as proton transport in proton exchange membranes is much slower than in aqueous electrolytes.[51] The SECCM technique described provides an effective way to investigate such an effect. Importantly, we demonstrate that it is possible to obtain approximate kinetic parameters for individual high-index grains in a semi-quantitative manner with a simple kinetic analysis.

Conclusions

SECCM combined with EBSD has allowed us to study electrode structure effects on the ORR at high-index facets of polycrystalline Pt with a three-phase boundary configuration. SECCM has provided information on variations in ORR activity across grains of different orientation at high spatial resolution. Grains having mixed (111) and (100) character exhibit higher activity than those with (100) and (110) features, in line with studies on pure single crystals, confirming the validity of our approach, while highlighting the versatility of the *pseudo single-crystal* approach as a means of investigating high-index crystal facets. Generally, the results on polycrystalline Pt highlight the importance of considering microstructural effects in order to understand the activity of practical electrocatalysts. In addition to illustrating the critical importance of grain structure, our results rule out major contributions to electrocatalytic activity from grain boundaries.

The approach described herein opens up new avenues for studying structure-activity relationships on complex surfaces. A key strength of the methodology is that it is underpinned by a quantitative treatment of mass transport,[27, 31] in this particular case we were able to elucidate the influence of the three-phase boundary and differential mass transport of oxygen and the products on the kinetics. In the future, we plan to integrate sensor electrodes into the SECCM probe that could be used to detect intermediates of electrode reactions. This could be particularly beneficial for the ORR reaction where the detection of H$_2$O$_2$ and other intermediates would provide deeper insight into microscopic kinetics, marrying the attributes of SECCM and scanning electrochemical microscopy.

Author information

[a] Department of Chemistry, University of Warwick, Gibbet Hill Rd, Coventry CV4 7AL, UK.; email: P.R.Unwin@warwick.ac.uk
[b] MESA+ Institute for Nanotechnology, University of Twente, PO Box 217, 7500 AE Enschede, The Netherlands

Electronic Supplementary Information (ESI) available: See DOI: 10.1039/b000000x/

References

1. A. Rabis, P. Rodriguez and T. J. Schmidt, *ACS Catal.*, 2012, **2**, 864-890.
2. B. Lim, M. Jiang, P. H. C. Camargo, E. C. Cho, J. Tao, X. Lu, Y. Zhu and Y. Xia, *Science*, 2009, **324**, 1302-1305.
3. B. C. H. Steele and A. Heinzel, *Nature*, 2001, **414**, 345-352.
4. C. O. Laoire, S. Mukerjee, K. M. Abraham, E. J. Plichta and M. A. Hendrickson, *J. Phys. Chem. C*, 2009, **113**, 20127-20134.
5. Y.-C. Lu, H. A. Gasteiger and Y. Shao-Horn, *J. Am. Chem. Soc.*, 2011, **133**, 19048-19051.
6. H. S. Wroblowa, P. Yen Chi and G. Razumney, *J. Electroanal. Chem.*, 1976, **69**, 195-201.
7. E. Yeager, *Electrochim. Acta*, 1984, **29**, 1527-1537.
8. A. A. Gewirth and M. S. Thorum, *Inorg. Chem.*, 2010, **49**, 3557-3566.
9. V. R. Stamenkovic, B. Fowler, B. S. Mun, G. Wang, P. N. Ross, C. A. Lucas and N. M. Marković, *Science*, 2007, **315**, 493-497.
10. V. Komanicky, H. Iddir, K.-C. Chang, A. Menzel, G. Karapetrov, D. Hennessy, P. Zapol and H. You, *J. Am. Chem. Soc.*, 2009, **131**, 5732-5733.

11. M. Nesselberger, S. Ashton, J. C. Meier, I. Katsounaros, K. J. J. Mayrhofer and M. Arenz, *J. Am. Chem. Soc.*, 2011, **133**, 17428-17433.

12. K. L. Hsueh, D. T. Chin and S. Srinivasan, *J. Electroanal. Chem.*, 1983, **153**, 79-95.

13. U. A. Paulus, A. Wokaun, G. G. Scherer, T. J. Schmidt, V. Stamenkovic, N. M. Markovic and P. N. Ross, *Electrochim. Acta*, 2002, **47**, 3787-3798.

14. N. M. Marković and P. N. Ross, Jr, *Surf. Sci. Rep.*, 2002, **45**, 117-229.

15. N. M. Marković, T. J. Schmidt, V. Stamenković and P. N. Ross, *Fuel Cells*, 2001, **1**, 105-116.

16. S. Guo, S. Zhang and S. Sun, *Angew. Chem. Int. Ed.*, 2013, **52**, 8526-8544.

17. M. D. Maciá, J. M. Campiña, E. Herrero and J. M. Feliu, *J. Electroanal. Chem.*, 2004, **564**, 141-150.

18. A. Kuzume, E. Herrero and J. M. Feliu, *J. Electroanal. Chem.*, 2007, **599**, 333-343.

19. N. M. Marković, R. R. Adžić, B. D. Cahan and E. B. Yeager, *J. Electroanal. Chem.*, 1994, **377**, 249-259.

20. N. M. Marković, H. A. Gasteiger and P. N. Ross, *J. Phys. Chem.*, 1995, **99**, 3411-3415.

21. N. M. Marković, H. A. Gasteiger and P. N. Ross, *J. Phys. Chem.*, 1996, **100**, 6715-6721.

22. F. El Kadiri, R. Faure and R. Durand, *J. Electroanal. Chem.*, 1991, **301**, 177-188.

23. H. Kita, H. W. Lei and Y. Gao, *J. Electroanal. Chem.*, 1994, **379**, 407-414.

24. A. Bandarenka, H. A. Hansen, J. Rossmeisl and I. Stephens, *Phys. Chem. Chem. Phys.*, 2014, DOI: 10.1039/C1034CP00260A.

25. O. V. Cherstiouk, A. N. Gavrilov, L. M. Plyasova, I. Y. Molina, G. A. Tsirlina and E. R. , *J. Solid State Electrochem.*, 2008, **12**, 497-509.

26. E. R. Savinova, F. Hahn and N. Alonso-Vante, *Surf. Sci.*, 2009, **603**, 1892-1899.

27. B. D. B. Aaronson, C.-H. Chen, H. Li, M. T. M. Koper, S. C. S. Lai and P. R. Unwin, *J. Am. Chem. Soc.*, 2013, **135**, 3873-3880.

28. D. W. Blakely and G. A. Somorjai, *Surf. Sci.*, 1977, **65**, 419-442.

29. N. Hoshi, S. Kawatani, M. Kudo and Y. Hori, *J. Electroanal. Chem.*, 1999, **467**, 67-73.

30. W. F. Banholzer and R. I. Masel, *J. Catal.*, 1984, **85**, 127-134.

31. N. Ebejer, A. G. Güell, S. C. S. Lai, K. McKelvey, M. E. Snowden and P. R. Unwin, *Annu. Rev. Anal. Chem.*, 2013, **6**, 329-351.

32. S. C. S. Lai, P. V. Dudin, J. V. Macpherson and P. R. Unwin, *J. Am. Chem. Soc.*, 2011, **133**, 10744-10747.

33. H. V. Patten, S. C. S. Lai, J. V. Macpherson and P. R. Unwin, *Anal. Chem.*, 2012, **84**, 5427-5432.

34. M. E. Snowden, A. G. Güell, S. C. S. Lai, K. McKelvey, N. Ebejer, M. A. O'Connell, A. W. Colburn and P. R. Unwin, *Anal. Chem.*, 2012, **84**, 2483-2491.

35. N. Ebejer, M. Schnippering, A. W. Colburn, M. A. Edwards and P. R. Unwin, *Anal. Chem.*, 2010, **82**, 9141-9145.

36. A. G. Güell, N. Ebejer, M. E. Snowden, J. V. Macpherson and P. R. Unwin, *J. Am. Chem. Soc.*, 2012, **134**, 7258-7261.

37. S. C. S. Lai, A. N. Patel, K. McKelvey and P. R. Unwin, *Angew. Chem. Int. Ed.*, 2012, **51**, 5405-5408.

38. A. G. Güell, N. Ebejer, M. E. Snowden, K. McKelvey, J. V. Macpherson and P. R. Unwin, *Proc. Natl. Acad. Sci. USA*, 2012, **109**, 11487-11492.

39. A. J. Schwartz, M. Kumar, B. L. Adams and D. P. Field, eds., *Electron Backscatter Diffraction in Materials Science*, Springer 2010.

40. M. F. Li, L. W. Liao, D. F. Yuan, D. Mei and Y.-X. Chen, *Electrochim. Acta*, 2013, **110**, 780-789.

41. M. J. Vasile and C. G. Enke, *J. Electrochem. Soc.*, 1965, **112**, 865-870.

42. V. Climent and J. M. Feliu, *J. Solid State Electrochem.*, 2011, **15**, 1297-1315.

43. B. D. B. Aaronson, S. C. S. Lai and P. R. Unwin, *Langmuir*, 2014, **30**, 1915-1919.

44. S. Chen and A. Kucernak, *J. Phys. Chem. B*, 2004, **108**, 3262-3276.

45. C. M. Zalitis, D. Kramer and A. R. Kucernak, *Phys. Chem. Chem. Phys.*, 2013, **15**, 4329-4340.

46. C. J. Slevin, S. Ryley, D. J. Walton and P. R. Unwin, *Langmuir*, 1998, **14**, 5331-5334.

47. L. Zitzler, S. Herminghaus and F. Mugele, *Phys. Rev. B*, 2002, **66**, 155436-155414.

48. J. Jang, G. C. Schatz and M. A. Ratner, *J. Chem. Phys.*, 2004, **120**, 1157-1160.

49. V. Komanicky, A. Menzel and H. You, *J. Phys. Chem. B*, 2005, **109**, 23550-23557.

50. O. V. Cherstiouk, A. N. Gavrilov, L. M. Plyasova, I. Y. Molina, G. A. Tsirlina and E. R. Savinova, *J. Solid State Electrochem.*, 2008, **12**, 497-509.

51. P. Choi, N. H. Jalani and R. Datta, *J. Electrochem. Soc.*, 2005, **152**, E123-E130.